Reconciling thermal regimes and tectonics of the early Earth

Capitanio*, F.A., Nebel, O. and Cawood, P.A. Weinberg, R.F. and Chowdhury, P.
School of Earth Atmosphere and Environment, Clayton, 3800 Vic, Australia
* corresponding author: fabio.capitanio@monash.edu

1. Numerical Modelling

1.1. Governing equations and numerical method

We model convection as the flow of a viscous fluid at very low Reynolds number in a two-dimensional Cartesian geometry solving the equations of conservation of mass, momentum and energy using the finite element code Underworld (Moresi et al., 2007). Underworld solves the equations using a finite element-particle in cell (FEM-PIC) scheme, that uses a Eulerian Finite Element Method where Lagrangian particles are embedded in the elements. This method allows to account for multi-material properties, which are then tracked throughout the history of the model. Using the Lagrangian particles we implement history-dependent melting and extraction, and the resulting rheological transition.

The equation of conservation of mass also enforces an incompressibility constrain:

$$\nabla \cdot \mathbf{u} = 0 \tag{1}$$

where $\mathbf{u}$ is the velocity vector, whereas the momentum conservation equation is:

$$\nabla \cdot \boldsymbol{\sigma} = \mathbf{f} \tag{2}$$

with $\boldsymbol{\sigma}$ the stress tensor and $\mathbf{f} = \rho \mathbf{g}$ the force term, with ρ the density and $\mathbf{g}$ the gravity.

The energy conservation equation is given by:

$$\frac{\partial \mathrm{T}}{\partial \mathrm{t}} + \mathbf{u} \cdot \nabla T = \kappa \nabla^2 T \tag{3}$$

with T the adiabatic temperature, t the time, κ the thermal diffusivity. The adiabatic temperature T is calculated as the following (Turcotte and Schubert, 1982):

$$T = T_{\mathrm{P}} + y \left(\frac{dT}{dy}\right)_{\mathrm{s}} = T_{\mathrm{P}} + y\, \alpha\, T \boldsymbol{g} / \mathrm{c_p} \tag{4}$$

Where T_{P} is the potential temperature, c_{p} is the heat capacity and all the other parameters are defined earlier. The stress tensor is split into a deviatoric term $\boldsymbol{\tau}$ and a (lithostatic) pressure p:

$$\boldsymbol{\sigma} = \boldsymbol{\tau} - p\mathbf{I} \tag{5}$$

where $\mathbf{I}$ is the identity tensor.

All materials' densities follow the same temperature-dependent law:

$$\rho = \rho_0 \left[1 - \alpha (T - T_0)\right] \tag{6}$$

where ρ_0 is the density at surface tempertature T_0, and α the coefficient of thermal expansion.

The constitutive equation for diffusion and dislocation viscous creep in materials is of the form:

$$\eta_{\text{diff, disl}} = D^{-\frac{1}{n}} \dot{\varepsilon}_{II}^{\frac{1-n}{n}} \exp\left(\frac{E + pV}{nRT}\right) \quad (7)$$

where η is the viscosity, $D = 0.5\, A\, \mu^{-n} (b/d)^{m}$ with A the pre-exponential factor, μ the shear modulus, b, d, and m the length of the Burgers vector, the grain size, and the grain size exponent, respectively, n the stress exponent, E the activation energy, V the activation volume, R the universal gas constant and $\dot{\varepsilon}_{II} = \sqrt{(\dot{\boldsymbol{\varepsilon}} : \dot{\boldsymbol{\varepsilon}})/2}$, the square root of the second invariant of the strain rate tensor:

$$\dot{\boldsymbol{\varepsilon}} = \frac{1}{2}[\nabla \mathbf{u} + (\nabla \mathbf{u})^{T}]. \quad (8)$$

The values of A, n, E and V are varied for diffusion and dislocation creep laws, η_{diff} and η_{disl} following parameters in Karato and Wu, 1993 (Table 1).

The creep viscosity is defined as the harmonic average of the two mechanisms:

$$\eta_{\text{creep}}^{-1} = \eta_{\text{diff}}^{-1} + \eta_{\text{disl}}^{-1}. \quad (9)$$

Pseudo-plastic flow of rocks is modelled implementing first a Drucker-Prager yield criterion:

$$\tau_Y = C_0 + p \sin \phi \quad (10)$$

with C_0 the cohesion at surface conditions and ϕ the internal friction angle. Then, we define plastic flow law through the definition of:

$$\eta_Y = \frac{\tau_Y}{2\dot{\varepsilon}_{II}}. \quad (11)$$

Finally, the composite visco-plastic rheology is as follows:

$$\eta^{-1} = \eta_{\text{creep}}^{-1} + \eta_Y^{-1}. \quad (12)$$

Symbol	Definition	Value	Unit
α	Thermal expansivity	3×10^{-5}	K^{-1}
$\boldsymbol{g}$	Gravitational acceleration	9.81	$m\,s^{-2}$
T_0	Surface temperature	0	$^\circ\ C$
T	Adiabatic temperature		$^\circ\ C$
c_p	Heat capacity	1000	$J\,kg^{-1}K^{-1}$
ρ_0	Density	3000	$kg\,m^{-3}$
κ	Thermal diffusivity	1×10^{-6}	$m^2\ s^{-1}$
η	Viscosity		$Pa\,s$
μ	Shear modulus	8×10^{10}	Pa
b	Burgers vector	5×10^{-10}	m
d	Grain size	10^{-3}	m
A_{diff}	Pre-exponential factor	6.0×10^{15}	s^{-1}
m_{diff}	Grain size exponent	2.5	
n_{diff}	Stress exponent	1.0	
E_{diff}	Activation energy	285×10^3	$J\,mol^{-1}$
V_{diff}	Activation volume	5	$cm^3\ mol^{-1}$
A_{disl}	Pre-exponential factor	1×10^{22}	$Pa\,s$
m_{disl}	Grain size exponent	0	
n_{disl}	Stress exponent	3.0	
E_{disl}	Activation energy	513×10^3	$J\,mol^{-1}$
V_{disl}	Activation volume	15	$cm^3\ mol^{-1}$
R	Universal gas constant	8.31	$J\,K^{-1}\ mol^{-1}$
τ_Y	Yield stress		MPa
C_0	Cohesion	60	MPa
ϕ	Internal friction	30	^{o}
F	Melting fraction		
X_{H2O}	Water content	$0.0, 0.05, 0, 1$	$wt\%$

Table 1. Symbols, definitions and values of the dimensional reference parameters used in this study, after Karato and Wu, 1993.

1.2. Melting and dehydration stiffening

Here, we focus on the rheological transition of such rocks undergoing melting and melt extraction. Melting is implemented as in other models addressing similar geodynamics problems (e.g., (Fischer and Gerya, 2016; Johnson et al., 2014; Sizova et al., 2015). We differ from these works, modelling weakening during melting production, we model the stiffening of the residue by melt, and fluid, extraction, the dehydration stiffening (e.g. Ballmer et al., 2011). The rheological stiffening that follows melt extraction is referred to as dehydration stiffening (Hirth and Kohlstedt, 2003; Korenaga, 2013), which is thought to be dominant in the lithosphere (Karato and Wu, 1993). We implement stiffening laws following the wet-to-dry transition of minerals as a result of melting, melt and fluid extraction resulting in increased viscosity (Mei and Kohlstedt, 2000).

We model the melt fraction F (T, p, X_{H2O}) as a function of the supersolidus temperature, pressure and water content, following McKenzie and Bickle, 1988, and Katz et al., 2003. The solidus and liquidus temperatures, T_{sol} and T_{liq}, are pressure-dependent and include melting of a hydrous mantle, bounded by the water saturated solidus T_{sat}:

$T_{\mathrm{sol}}\,(p) \rightarrow T_{\mathrm{sol}}\,(p) - \Delta T(X_{\mathrm{H2O}})$

$$T_{\mathrm{liq}}(p) \rightarrow T_{\mathrm{liq}}(p) - \Delta T(X_{\mathrm{H2O}})$$

We consider here a closed system, that is the net water content does not change with time (Korenaga, 2013), and model rheological transitions only for dehydrated rocks, following melt extraction, so that we do not differentiate melt or bulk water content.

Defining a dimensionless super-solidus temperature as:

$$T' = \frac{T - (T_{\mathrm{sol}} - T_{\mathrm{liq}})/2}{T_{\mathrm{liq}} - T_{\mathrm{sol}}} \tag{13}$$

we then calculate the melt fraction F as:

$$F = a + T' + (T'^2 - b)(c + d\,T') \tag{14}$$

with $a = 0.5$, $b = 0.25$, $c = 0.4256$ and $d = 2.988$ (McKenzie and Bickle, 1998).

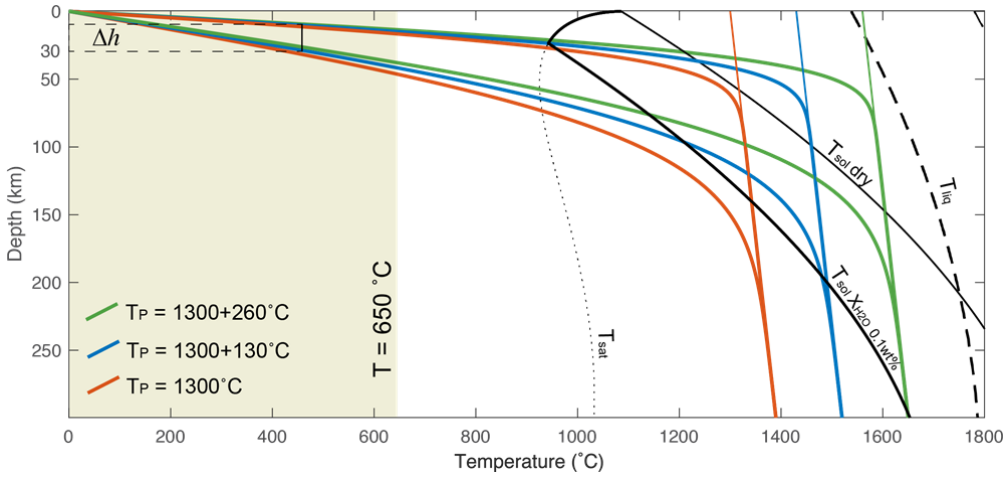

Fig. S1. Schematic melting as a function of temperature and depth for different domains and potential temperatures, for depth y < 300 km. Materials that undergo melting achieving different amount of melt extraction and dehydration. Similar melt fractions occur under increased T_{P} or increased water contents. Rheological transition of materials occurs when these reach sub-solidus temperatures. For clarity, the differentiated materials in the models are shown when reaching lithosphere-crust temperature, T < 650 ˚C, where residual rocks are considered emplaced in the lithosphere (shaded area). Thinning Δh is calculated along the isotherm corresponding to an initial depth of 30 km. Solidii and liquidii after Katz et al., 2003.

In the models, the melt fraction is calculated for every point on the Lagrangian particles as F, then it is progressively subtracted during each melting episode to yield the total dehydration M. Melt extracted and associated volumetric variations are not modelled: the melt is considered extracted instantaneously and emplaced on top, that is out of the model, i.e. eruption efficiency of

100%, while no volumetric variations is implemented in order not to violate the enforced mass conservation criterion, eq. (1). This is a value assumed for the Archean in the heat-pipe mode (Moore and Webb, 2013), although it might have been as low as 40% (Rozel et al., 2017). In order to keep the models in the same regime throughout their evolution, we do not embed secular cooling, nor any other cooling mechanism, such as those proposed by Rozel et al., 2017.

The dehydration function M is calculated as the difference between melt fraction F_n at the summation of melt extraction events prior to the event n, during the model run:

$$M = F_{\mathrm{n}} - \sum_{\mathrm{i}=1}^{\mathrm{n}-1} M_{\mathrm{i}} \quad (15)$$

This is implemented following previous modelling efforts (e.g., (Sizova et al., 2015). The inferred Archean conditions for melt and crust formation imply high degrees of mantle melting, over a range of mantle pressures of Δp = 2–10 GPa, with melt fractions as large as 0.3 to 0.44 (Herzberg et al., 2010). Hence, equation (15) is defined for $M \leq 0.44$, which is the maximum melt extraction allowed in the models.

Dehydration stiffening is modelled following the wet-to-dry transition of mantle forming mineral Olivine (Karato and Wu, 1993; Mei and Kohlstedt, 2000). An empirical law commonly used to express melt-dependent viscosity variations is of the form $\eta = \eta_0(1 - M)\exp(\alpha M)$ (e.g., Dunnberg and Heister, 2016; Keller et al., 2013), where the second term in the r.h.s. expresses the volume fraction and the third the viscosity change, with α a constant. This equation captures the viscosity drop of several orders of magnitude as melt is produced, while the viscosity of the residue increases, through the wet-to-dry transition. Here, we use the same equation to express the residual viscosity increase, modified to account for the solid-liquid viscosity ratio increase, best expressed by a non-linear function of the melt fraction, the Einstein-Roscoe equation:

$$\eta_{\mathrm{diff,\,disl}}(M) = \eta_{\mathrm{diff,\,disl}} \left(1 - \frac{M}{M_{\mathrm{max}}}\right)^{-2.5} \exp(\alpha M) \quad (16)$$

The Einstein-Roscoe equation provides an empirical fit to a range of viscosity measurements ranging from basalts to olivine as a function of melt fraction, for low and intermediate melt fractions, with $1/M_{\mathrm{max}}$ = 1.35 (see Kohlstedt and Hansen, 2015; Pinkerton and Stevenson, 1992) and references therein), and α = 5.7 to limit the magnitude of melt viscosity increase (e.g., Dunnberg and Heister, 2016). In figure S2 we show the stiffening resulting from these different terms, showing that largest viscosity increase is ~10^2. Although the magnitude of the stiffening is debated, this value is in agreement with a wealth of laboratory measurements (e.g., Karato and Wu, 1993; Kohlstedt and Hansen, 2015; Mei and Kohlstedt, 2000).

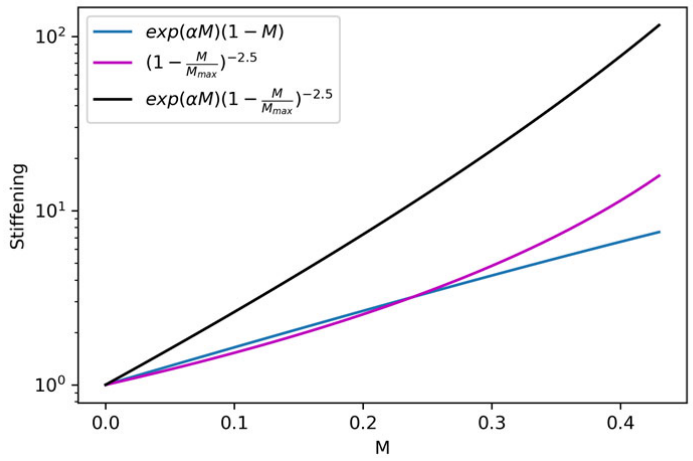

Fig. S2. Viscosity increase (stiffening) as a function of melt fraction M, for $M \leq 0.44$. The exponential function (blue) and the Einstein-Roscoe equation (magenta) yield similar stiffening increase. Combining the two terms in the equation used here (black), yields a viscosity increase up to a factor 10^2.

In our models the density variation with melting is not accounted for. The buoyancy increase due to depletion of the lithosphere is estimated to vary linearly by 0.726 kg m^{-3} per depletion percent (Schutt and Lesher, 2006), although estimates may range between 3 and 0 kg m^{-3} per depletion percent. For largest melting in the Archean this implies $\Delta\rho$ <32 kg m^{-3}, that is $\Delta\rho/\rho \sim 10^{-2}$, over thick lithospheric mantle layers. On the other hand, this might be balanced by the eclogitization of a ~30 km thick crust, with an increase of $\Delta\rho$ ~300 kg m^{-3}, that is $\Delta\rho/\rho \sim 10^{-1}$. The role of the density variations is critical for the viability of subduction in the early Earth (Davies, 2005), although these mechanisms results in density variations that likely cancel each other (van Hunen and Moyen, 2012). Additionally, we do not address the emergence of plate tectonics nor subduction here, thus such buoyancy variations are ignored.

1.3. Model setup

We model convection the upper mantle in a space of 660 × 6600 km, discretized in 64 × 640 elements, embedding a total of 819200 Lagrangian particles. We enforce free-slip boundary condition slip on all the boundaries.

The initial temperature distribution is fixed at T_0 on the top and T_P on the bottom model boundaries, respectively. The model is run for an initial 1000 Myr by which time steady-state is

achieved (Rey et al., 2014). Then, we average the temperature and setup an initial profile simulating a uniform thermal boundary and introduce a thinning in the model's trailing 330 km (Fig. S3), where the isotherms $T < 0.85\ T_P$ are tapered. This results in a thinning of the lithosphere, Δh, which is measured here as the maximum shallowing of the isotherm corresponding to an initial depth of 30 km (Fig. S3, B), a likely value for the Archean crust (van Hunen and Moyen, 2012), measured in x = 6600 km. This is a measure of isotherm uplift and, therefore, of whole lithosphere thickness variation (Fig. S1). Because of the model's supercritical Rayleigh number $Ra = \sim 10^6$, the boundary layer evolves rapidly, as the simulation starts and the convection pattern establishes, giving rise to a convection-controlled boundary layer thickness.

We have run a total of 36 models, varying values of melt water content X_{H2O} = 0.0, 0.05 and 0.1 wt%, and initial thinning Δh = 0, 10, 15, 20 km, each one with temperature increase of ΔT = 0, +130 and +260˚C. The water content of the mantle is debated, water content of normal MORB is ~0.04-0.20 % (see Herzberg et al., 2007). Because MORB is the result of ~10 % mantle partial melting, assuming a linear dependence, a partial melting of 40-50 % in the Archean (see Herzberg et al., 2007) would result in a maximum water content of the source mantle of <0.88 %. (Korenaga, 2018) suggests a dry early Earth mantle, thus providing a minimum value. The modelled water content brackets these values. The values of thinning are below the thickness of the Archean crust, thus resulting in rifting, yet no break-up follows.

The melting in the models is achieved by decompression beneath the thinned areas. In the models this is a function of the initial mantle water content, potential temperatures, and lithospheric thinning, and expresses the geotherm height above the solidus. In figure S1 a range of different geotherms and water contents illustrate that the height of the geotherm above the solidus, and thus the melting fraction, can be the same under different conditions. This allows presenting the models outcomes grouped.

The plasticity parameters are chosen to ensure the models does not transition to other regimes, through yielding of the lid, and therefore do not play a role in our models. The regime transition remains highly debated and is beyond the goal of our work. Instead, we address the evolution within the same regime, here.

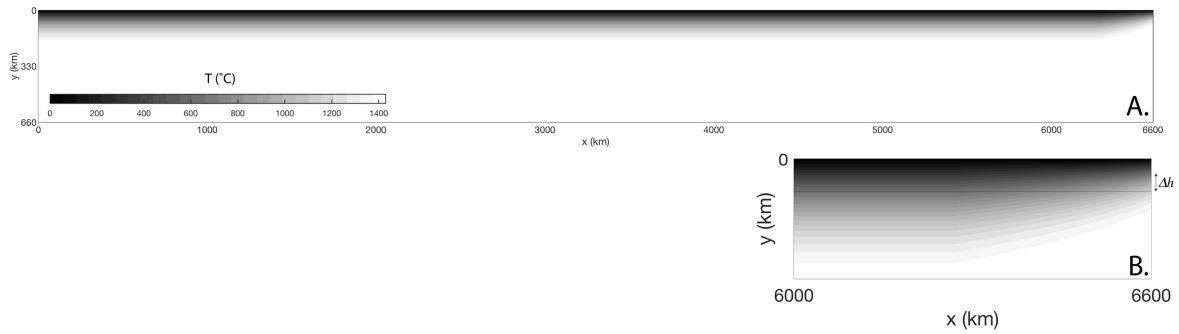

Fig. S3. Initial potential temperature distribution. A. The top boundary layer is uniform throughout the model, except in the 330 km on the right-hand side. B. Enlargement of the temperature distribution in the dashed line box in A. Isotherms are tapered, resulting in a thinning Δh, measured along the $T = 650$ ˚C isotherm.

1.4. Initial conditions

The initial conditions used here are based on two assumption: 1) an existing boundary layer and 2) a localized thinned lithosphere. The initial boundary layer is commonly used in planetary modelling (e.g., Fischer and Gerya, 2016; Rozel et al., 2017) and in many studies addressing tectonics of the early Earth (e.g., Rey et al., 2014; Sizova et al., 2015). The localised thinning mimics conditions of divergent commonly achieved in many regimes, from stagnant to sluggish lid regimes and plate tectonics. In the pre-plate tectonics regimes, lithospheric drips develop above down-wellings. By virtue of the mass conservation principle, thickening above down-wellings must be balanced by thinning elsewhere. Stable ridge formation is reported in the work of Rozel et al., 2015, and similarly occurs in the work of O'Neill et al., 2007, although transient. Geological evidence of rifting is reported in many cases, e.g. the Pilbara craton at ~3.2 Ga (Van Kranendonk et al., 2007), and in the Isua belt at ~3.8 Ga (Furnes et al., 2007). Similarly, thinning of a rigid lithosphere can be the consequence of mantle plume-lithosphere interactions (Fischer and Gerya, 2016). Other mechanisms could be responsible for localized thinning, such as the role of impacts in the Hadean (O'Neill et al., 2017). It has to be noted that this assumption might not stand in a heat-pipe early Earth mode, where the lithosphere would remain mostly uniform and vertical resurfacing events would control the cooling mode (Moore and Webb, 2013). Yet, which of these styles best explain the early Earth conditions remains an open debate.

1.5. Model evolutions

We present the modelling outcomes grouped in maximum melt achieved in the site of thinning. This depends on a trade-off between the geotherm perturbation, i.e. the thinning, and the maximum

potential temperature and the water content. These parameters define the relative height of the geotherm above the solidus (fig. S1) and therefore are all expressed by the maximum melting fraction *X*. Consequently, the modelling outcomes remain less dependent on the chosen water content and thinning. For sake of clarity, we only show here three type of models, all with similar water content and temperature increase, only the thinning is varied.

1.5.1. *Uniform initial boundary layer,* $\Delta h = 0$

Under all modelled potential temperatures, i.e. ΔT = 0, +130 and +260˚C, and with no change in initial model's boundary layer thickness, Δh = 0, mantle convection develops beneath a poorly mobile lithosphere - the stagnant lid - into regularly-spaced, low aspect ratio, convecting cells (Fig. S4). Melt only forms at the bottom of the boundary layer, under super-solidus *T*-*P* conditions. However, because of the temperature-dependence of viscosity, the behaviour of the melt-bearing rocks is indistinguishable from the background mantle at these large temperatures, i.e. dehydration stiffening is negligible. In these models, a stable mantle convection pattern develops in ~ 600 Myr. The pattern is very similar for the potential temperatures tested, and we only show one in Figure S4 for reference. Dehydrated material is located at the bottom of the lid, and is partially recycled back to the mantle within ~200 Myr along sub-vertical drips beneath the lithosphere (Fig. S4, B, C).

Varying mantle potential temperature and water content affect the rheology, and therefore, the size of cells in the models as well as the timescales of convection. However, in all these models the stagnant lid regime is maintained.

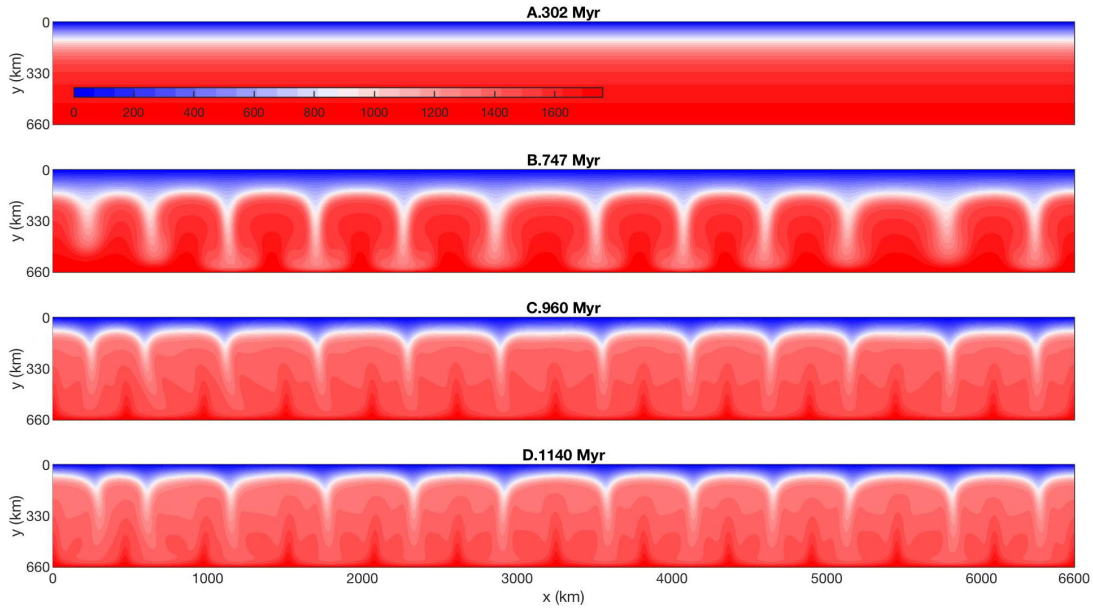

Figure S4. Model with no initial thinning developing a stable pattern of convection beneath a rather stagnant lid.

1.5.2. Initially thinned boundary layer and moderate melting fraction, $\Delta h > 0$ and $X<\sim0.2$

In models where moderate thinning is modelled as an initial condition and potential temperature difference is moderate, i.e. Δh = 10 km and ΔT = +130 ℃, the melting fraction does not raise above X = ~0.2 (Fig. S5) and therefore the dehydration stiffening is moderate. In these models, two domains develop within the lid, as in those presented in the manuscript, however, the stability conditions are not met, and the pattern is transient until the modelled time of ~1 Gyr (Fig. S5, D).

In these models, the initial thinning perturbation triggers lateral motions. Here, the laterally migrating lithosphere develops, and drags laterally the drips in the early stage of the models (< 486 Myr, Fig. 4, A, B), forcing a longer wavelength planform to underlying convection. On the other end of the model, the left-hand side, a stagnant lid develops (Fig. 4, left), where a pattern of closely spaced convecting cells forms beneath a rather immobile lid, with lithospheric drips beneath. However, the negligible dehydration stiffening in these models prevent the models to enter steady-state, the mobile lid domain does not grow largely, and then reverts to a rather poorly mobile lithosphere. Large down-welling formed are not stable and reorganize with time.

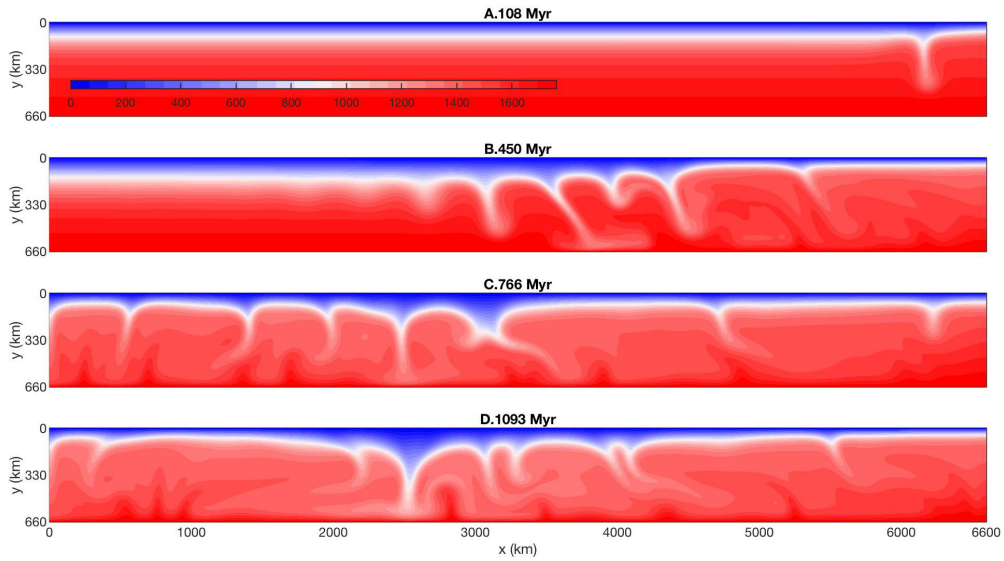

Figure S5. Model with small initial thinning with small amount of melting, X<~0.2, develops a transient pattern of convection with transient down-wellings.

1.5.3. Initially thinned boundary layer and large melting fraction, $\Delta h > 0$ and X>~0.2

In models with an increase of potential temperature, $\Delta T = +130^{\circ}$C, and larger thinning is imposed, Δh = 20 km, the melt fraction raises to a maximum of X = ~0.45, thus dehydration stiffening is maximized. Two domains develop as in the previous models, although the patter established earlier and is remains stable.

This model evolves in a similar way to the previous model, with the left side showing regularly-spaced, low aspect ratio, convecting cells beneath a poorly mobile lithosphere of constant thickness (stagnant lid) (Fig. S6). Along the locus of lithospheric thinning, on the right wall of the model, shallow melting beneath the thinned lithosphere and melt extraction results in the progressive dehydration stiffening of the lithosphere (right in Fig. S6). Larger amount of melt fraction and melt extraction result in stiffer layers in the lithosphere, as a consequence, the lithosphere stabilizes rapidly, reaching ~3000 km, then becoming a feature of the system.

The enhanced forcing of the proto-plate onto the drips results in dragging and tilting the sub-lithospheric drips (Fig. 6, A, B). The stiffened, migrating portion of the lithosphere pushes several of drips towards the stagnant lid, which is progressively compressed and thickens, until a large lithospheric down-welling instability forms along the margin between the two domains by ~700 Myr (Fig. S6, C). The thickening of the stagnant lid acts to reducing the further widening of the proto-plate, to a width of ~3000 km, achieving stress balance around the margin.

The overall increased rigidity of proto-plates results in stably migrating asymmetric drips, and the suppression of the stagnant lid-like vertical drips beneath the proto-plate (Fig. S6, D).

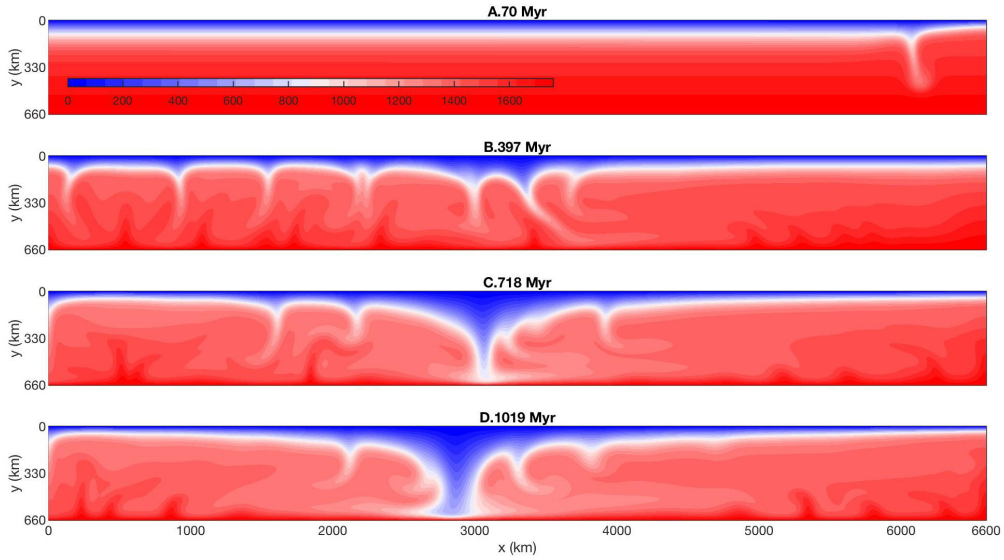

Figure S6. Model with larger initial thinning and larger amount of melting, X>~0.2, develops rapidly a stable pattern of convection with a stationary large lithospheric down-welling.

1.6. Equilibrium conditions

All models' evolution achieves an equilibrium condition when the proto-plate widens to width of ~3000 km (Fig. S7). At this point the velocity of the convergent zone drops to 0, when this does not migrate anymore. This condition implies that the horizontal forces around the 0-velocity point, $x' = 0$, are balanced, that is the two side apply a force equal and opposite $F_x = \int_h \sigma_{xx}(y)dy = 2\int_h \dot{\varepsilon}_{xx}(y)\eta(y)dy$, with σ_{xx} the horizontal stress, $\dot{\varepsilon}_{xx}$ the horizontal strain rate and η the viscosity. A model with a piece-wise constant values allows illustrating the concept sketched in figure S7, where the force balance arund $x' = 0$ becomes:

$$2\dot{\varepsilon}_{xx}\,\eta_{pp}h_{pp} = -2\dot{\varepsilon}_{xx}\,\eta_{pc}h_{pc} \quad (17)$$

with subscript pc for the proto-continent and pp for the proto-plate. Because the velocity field is continuous across the convergent zone, the strain rate on $x' = 0^+$ and $x' = 0^-$ does not vary, then:

$$\eta_{pp}/\eta_{pc} = h_{pc}/h_{pp}. \quad (18)$$

In the models the thickening of a proto-craton is of a factor ~2-4 with respect to the proto-plate, hence the intergrated viscosity increase in this latter is estimated of a similar factor. This point is, in the models, where the strain rate is maximised, showing that this area is also localizing large stress.

It is likely that the stress in this point would eventually result in a subduction zone forming. However, whether this occurs, when and under which conditions is out of the goal of this work.

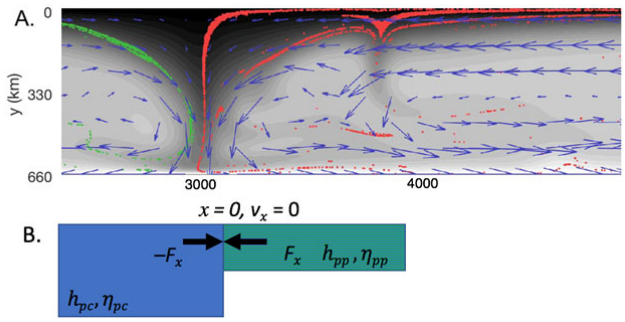

Figure S7. A schematic representation of the boundary between the thin and thick lithosphere. A) model from figure 1. B) Schematic representation of A. Because the point $x' = 0$ does not move in time (figures 1, 2), the force around it balance, so that $F_x = -F_x$. Subscripts pc and pp for the proto-plate (green) and proto-craton (blue), h and η for thickness and viscosity, respectively.

As the models reach an equilibrium, two different stable types of geotherms develop, one in the thinner lithosphere domain, and other in the thicker domain (Fig. S8). These equilibrium geotherms are in agreement with the work of Cooper et al., 2004; Lenardic and Moresi, 2000 and support the idea of two heat flow domains in agreement with Lenardic, 1998.

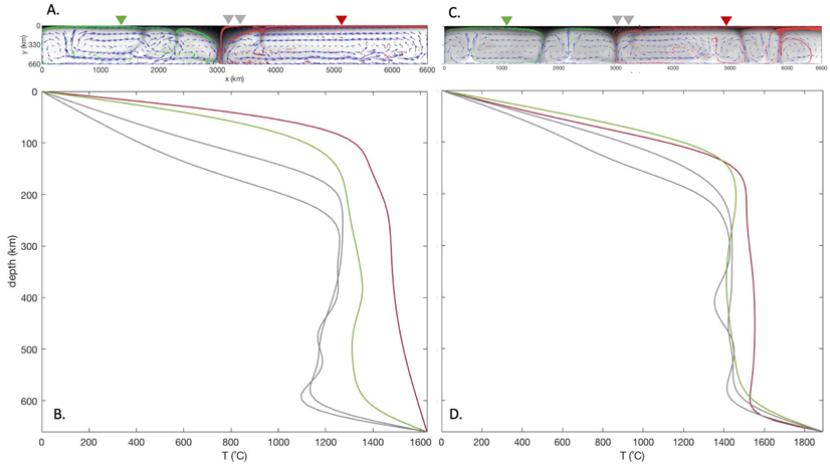

Figure S8. Example of geotherms in the models. (A) Model with $\Delta T = +130$ ˚C, with geotherms in the thinned domain (red triangle), thinned domain under stagnant lid (green) and thickened domain (grey). (B) Geotherms from (A) show the coexistence of hotter geotherms (red and green) as opposed to colder stable geotherms (grey). (C) In the model with $\Delta T = +260$ ˚C, the different geotherms develop similarly, yet (D) the difference between the thinned domains (red and green)

are minor and the temperature difference at depth, beneath the downwelling are less pronounced (grey).

1.7 Crustal formation and reworking

The crustal recycling in the models is calculated only for the domain on the right-hand side, that is for the red particles, which is the most mobile domain. Formation of new crust and its recycling in the left hand-side model is, essentially, 0, as no mechanism for deep burial emerges here.

We measured crust using a non-dimensional parameter Φ, modified from Chowdhury et al., 2017:

$$\Phi_{N,R} = V_{N,R} / V_0 \quad (19)$$

Where the subscript N and R are for new crust formation and recycled crust, respectively, V is the crust volume and V_0 is the initial model volume. The new crustal volume is the volume of the material undergone melting and reaching subsurface conditions (depth <40 km). All the crustal material that is buried to depth > 60 km and is at $T < T_{sol}$ is considered reworked. The material passing the threshold of T_{sol} is considered recycled in the mantle. Additionally, we calculated the percentage of crustal reworking to the total crust. Although this is a crude estimation of the volumes, it provides relative values that can be used comparatively among the models.

Figure S9 shows that all the curves have a similar trend with an initial increase of new crust formed reaching a plateau within <~250 Myr, following the onset of the crust-forming mechanism, at site of lithospheric thinning. The rate of crust formation remains rather constant until the lithospheric down-welling increases the mobility, thereby increasing the rate of new crust formation. This peaks between 500 and 700 Myr for models with ΔT = +130 ˚C, and 800-900 Myr for models with ΔT = +260 ˚C. In all models tested the new crust formation, then, decreases as the model stabilises. In models with ΔT = +130 ˚C the following decrease is larger, while in models with largest temperature difference, the new crust formation rate decay slowly.

The onset of the down-welling coincides with the progressive crustal recycling, with steadily increasing values in all models. The percentage of crustal reworking has a two-step increase, one coinciding with the first crustal formation the second is reached as the crust is recycled, then drawn back in the mantle. In all models, crustal reworking reaches ~8% initially, then reaching 20 - 30% after ~500 Myr since the model inception. While this stabilizes in models with ΔT = +130 ˚C, it progressively increases to ~40% in the models with the largest temperature difference tested.

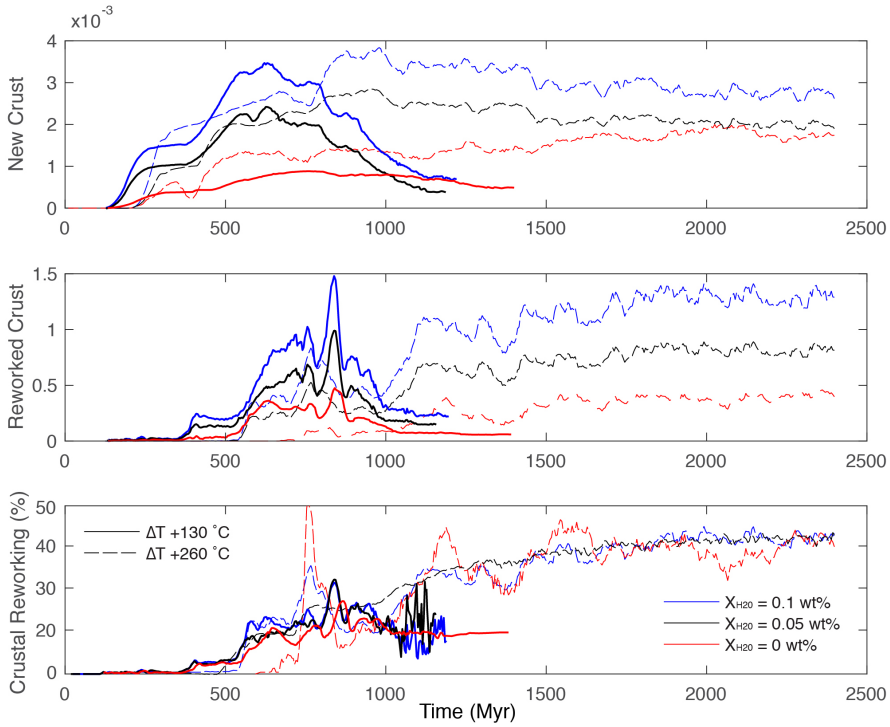

Figure S9. Model calculated (A) new crust formation and (B) reworking. The ratio of crustal reworking to the total is expressed in percent (C).

References

Ballmer, M. D., Ito, G., van Hunen, J., and Tackley, P. J., 2011, Spatial and temporal variability in Hawaiian hotspot volcanism induced by small-scale convection: Nat. Geoscience, v. 4, p. 457-460.

Chowdhury, P., Gerya, T. V., and Chakraborty, S., 2017, Emergence of silicic continents as the lower crust peels o on a hot plate-tectonic Earth: Nat. Geoscience, v. 10, p. 698-703.

Cooper, C. M., Lenardic, A., and Moresi, L., 2004, The thermal structure of stable continental lithosphere within a dynamic mantle: Earth Plan. Sci. Lett., v. 222, p. 807-817.

Davies, G. F., 2005, On the emergence of plate tectonics: Geology, v. 20, p. 963-966.

Dunnberg, J., and Heister, T., 2016, Compressible magma/mantle dynamics: 3-D, adaptive simulations in ASPECT: Geophys. J. Int., v. 207, p. 1343-1366.

Fischer, R., and Gerya, T. V., 2016, Early Earth plume-lid tectonics: A high-resolution 3D numerical modelling approach: J. Geodyn., v. 100, p. 198-214.

Furnes, H., De Wit, M., Staudigel, H., Rosing, M., and Muehlenbachs, K., 2007, A vestige of Earth's oldest ophiolite: Science, v. 315, p. 1704–1707.

Herzberg, C., Asimow, P. D., Arndt, N., Niu, Y., Lesher, C. M., Fitton, J. G., Cheadle, M. J., and Saunders, A. D., 2007, Temperatures in ambient mantle and plumes: constraints from basalts, picrites, and komatiites: Geochem. Geophys. Geosys., v. 8, no. 2.

Herzberg, C., Condie, K., and Korenaga, J., 2010, Thermal history of the Earth and its petrological expression: Earth Plan. Sci. Lett., v. 292, p. 79–88.

Hirth, G., and Kohlstedt, D. L., 2003, Rheology of the upper mantle and the mantle wedge: a view from the experimentalists, Inside the Subduction Factory, Volume 138: Washington D. C., Geophysical Monograph American Geophysical Union, p. 83-105.

Johnson, T. E., Brown, M., Kaus, B. J. P., and VanTongeren, J. A., 2014, Delamination and recycling of Archaean crust caused by gravitational instabilities: Nat. Geoscience, v. 7, p. 47-52.

Karato, S. I., and Wu, P., 1993, Rheology of the upper mantle - A sythesis: Science, v. 260, no. 5109, p. 771-778.

Katz, R. F., Spiegelman, M., and Langmui, C. H., 2003, A new parameterization of hydrous mantle melting: Geochem. Geophys. Geosys., v. 4, no. 9, p. doi:10.1029/2002GC000433.

Keller, T., May, D. A., and Kaus, B. J. P., 2013, Numerical modelling of magma dynamics coupled to tectonic deformation of lithosphere and crust: Geophys. J. Int., v. 195, no. 3, p. 1406-1442.

Kohlstedt, D. L., and Hansen, L. N., 2015, Constitutive Equations, Rheological Behavior, and Viscosity of Rocks, *in* Schubert, G., ed., Treatise on Geophysics, Volume 2, p. 441-472.

Korenaga, J., 2013, Initiation and Evolution of Plate Tectonics on Earth: Theories and Observations: Annu. Rev. Earth Planet. Sci., v. 41, p. 117-151.

-, 2018, Crustal evolution and mantle dynamics through Earth history: Phil. Trans. R. Soc. A, v. 376, p. http://dx.doi.org/10.1098/rsta.2017.0408.

Lenardic, A., 1998, On the partitioning of mantle heat loss below oceans and continents over time and its relationship to the Archaean paradox: Geophys. J. Int., v. 134, no. 3, p. 706-720.

Lenardic, A., and Moresi, L. N., 2000, A new class of equilibrium geotherms in the deep thermal lithosphere of continents: Earth Plan. Sci. Lett., v. 176, p. 331-338.

McKenzie, D., and Bickle, M. J., 1998, The Volume and Composition of Melt Generated by Extension of the Lithosphere: J. of Petrology, v. 29, no. 3, p. 625-679.

Mei, S., and Kohlstedt, D. L., 2000, Influence of water on plastic deformation of olivine aggregates: J. Geophys. Res, v. 105, p. 21457-21469.

Moore, W. B., and Webb, A. G., 2013, Heat-pipe Earth: Nature, v. 501.

Moresi, L., Quenette, S., Lemiale, V., C., M., Appelbe, B., and Mülhaus, H. B., 2007, Computational approaches to studying non-linear dynamics of the crust and mantle: Phys. Earth Plan. Int., v. 163, no. 1-4, p. 69-82.

O'Neill, C., Marchi, S., Zhang, S., and Bottke, W., 2017, Impact-driven subduction on the Hadean Earth: Nat. Geoscience, v. 10, p. 793-797.

Pinkerton, H., and Stevenson, R. J., 1992, Methods of determining the rheological properties of magmas at subliquidus temperatures: J. Volc. Geother. Res., v. 53, p. 47-66.

Rey, P. F., Coltice, N., and Flament, N., 2014, Spreading continents kick-started plate tectonics: Nature, v. 513, p. 405-408.

Rozel, A. B., Golabek, G. J., Jain1, C., Tackley, P. J., and Gerya, T. V., 2017, Continental crust formation on early Earth controlled by intrusive magmatism, v. 545, p. 332 - 335.

Schutt, D. L., and Lesher, C. E., 2006, Effects of melt depletion on the density and seismic velocity of garnet and spinel lherzolite: J. Geophys. Res., v. 111, p. B05401.

Sizova, E., Gerya, T. V., Stüwe, K., and Brown, M., 2015, Generation of felsic crust in the Archean: A geodynamic modeling perspective: Precambrian Res., v. 2771, p. 198-224.

Turcotte, D. L., and Schubert, G., 1982, Geodynamics, application of continuum mechanics to geological problems, New York, John Wiley & Sons.

van Hunen, J., and Moyen, J. F., 2012, Archean Subduction: Fact or Fiction?: Annu. Rev. Earth Planet. Sci. , v. 40, p. 195–219.

Van Kranendonk, M. J., Smithies, R. H., Hickman, A. H., and Champion, D. C., 2007, Secular tectonic evolution of Archean continental crust: interplay between horizontal and vertical processes in the formation of the Pilbara Craton, Australia: Terra Nova, v. 19, no. 1, p. 1-38.